DTIC COPY

REPORT DOCUMENTATION PAGE

Form Approved
OMB No. 0704-01-0188

PLEASE DO NOT RETURN YOUR FORM TO THE ABOVE ADDRESS.

1. REPORT DATE *(DD-MM-YYYY)*	2. REPORT TYPE	3. DATES COVERED *(From - To)*
17-06-2009	REPRINT	

4. TITLE AND SUBTITLE

Energy and power requirements of the global thermosphere during the magnetic storm of November 10, 2004

5a. CONTRACT NUMBER

5b. GRANT NUMBER

5c. PROGRAM ELEMENT NUMBER
62601F

5d. PROJECT NUMBER
2301

5e. TASK NUMBER
SD

5f. WORK UNIT NUMBER
A5

6. AUTHORS

W. J. Burke*
Cheryl Y. Huang
D. R. Weimer**
J. O. Wise
G. R. Wilson
C. S. Lin
F. A. Marcos

7. PERFORMING ORGANIZATION NAME(S) AND ADDRESS(ES)

Air Force Research Laboratory /RVBXP
29 Randolph Road
Hanscom AFB, MA 01731-3010

8. PERFORMING ORGANIZATION REPORT NUMBER
AFRL-RV-HA-TR-2010-1079

9. SPONSORING/MONITORING AGENCY NAME(S) AND ADDRESS(ES)

10. SPONSOR/MONITOR'S ACRONYM(S)
AFRL/RVBXP

11. SPONSOR/MONITOR'S REPORT NUMBER(S)

12. DISTRIBUTION/AVAILABILITY STATEMENT
Approved for public release; distribution unlimited.

13. SUPPLEMENTARY NOTES Reprinted From: Journal Atmospheric and Solar-Terrestrial Physics, Vol. 72 (2010), 309-318

*Boston College Institute for Scientific Research, Chestnut Hill, MA 02467
**Virginia Polytechnic Institute and State University, National Institute of Aerospace, Hampton, VA 23666

14. ABSTRACT

We used Poynting fluxes and densities $\bar{\rho}$ to investigate the stormtime thermosphere on November 10, 2004. Thermospheric energy E_{th}, which is derived from $\bar{\rho}$, consists of two sources, solar ultraviolet radiation ($E_{th\ uv}$) and the solar wind ($E_{th\ sw}$). Responses of $E_{th\ sw}$ to interplanetary driving suggest that the thermosphere can be described by the equation $d E_{th\ sw}/dt = \alpha\varepsilon_{vs} - (E_{th\ sw}/\tau)$, where ε_{vs} represents the electric field; α and τ are constants. We show that: (1) $E_{th\ sw}$ is three times the ring-current energy; (2) $\alpha\varepsilon_{vs}$ is comparable with model predictions; (3) signatures of equatorward propagating disturbances were detected in neutral density profiles.

15. SUBJECT TERMS

Magnetic storm Poynting flux Thermospheric energy

16. SECURITY CLASSIFICATION OF:			17. LIMITATION OF ABSTRACT	18. NUMBER OF PAGES	19a. NAME OF RESPONSIBLE PERSON
a. REPORT	b. ABSTRACT	c. THIS PAGE			Cheryl Huang
UNCL	UNCL	UNCL	UNL	9	19B. TELEPHONE NUMBER *(Include area code)*

Journal of Atmospheric and Solar-Terrestrial Physics 72 (2010) 309–318

Contents lists available at ScienceDirect

Journal of
Atmospheric and Solar-Terrestrial Physics

journal homepage: www.elsevier.com/locate/jastp

Energy and power requirements of the global thermosphere during the magnetic storm of November 10, 2004

W.J. Burke [a,b], C.Y. Huang [a,*], D.R. Weimer [c], J.O. Wise [a], G.R. Wilson [a], C.S. Lin [a], F.A. Marcos [a]

[a] Air Force Research Labaratary, Space Vehicles Directarate, 29 Rondolph Rd., Hanscam AFB, MA 01731-3010
[b] Bostan College Institute for Scientific Research, 140 Commonweolth Ave., Chestnut Hill, MA 02167
[c] Virginia Polytechnic Institute and State University, National Institute of Aerospace, Hamptan VA 23666

ARTICLE INFO

Article history:
Accepted 4 June 2009
Available online 17 June 2009

Keywords:
Magnetic storm
Poynting flux
Thermospheric energy

ABSTRACT

We used Poynting fluxes and densities $\tilde{\rho}$ to investigate the stormtime thermosphere on November 10, 2004. Thermospheric energy, E_{th} which is derived from $\tilde{\rho}$, consists of two sources, solar ultraviolet radiation ($E_{th\ UV}$) and the solar wind ($E_{th\ SW}$). Responses of $E_{th\ SW}$ to interplanetary driving suggest that the thermosphere can be described by the equation $dE_{th\ SW}/dt = \alpha\varepsilon_{VS} - (E_{th\ SW}/\tau)$, where ε_{VS} represents the electric field; α and τ are constants. We show that: (1) $E_{th\ SW}$ is three times the ring-current energy; (2) $\alpha\varepsilon_{VS}$ is comparable with model predictions; (3) signatures of equatorward propagating disturbances were detected in neutral density profiles.

Published by Elsevier Ltd.

1. Introduction

Quantifying the energy content of the coupled magnetosphere–ionosphere–thermosphere (MIT) system during geomagnetic storms is a long sought goal of space weather research. The Dessler–Parker–Sckopke (DPS) theorem argues that the total energy of ring-current (E_{RC}) particles is directly proportional to the Dst index (cf. review by **Carovillano and Siscoe, 1973**). The Assimilative Mapping of Ionospheric Electrodynamics (AMIE) technique (**Richmond and Kamide, 1988**) combines data from ground and satellite-borne sensors to reconstruct electric fields (ε) and current ($\mathbf{j}$) patterns at high latitudes. In its simplest representation energy into the ionosphere–thermosphere (IT) takes the form of Joule heat $= \sum_P \cdot \varepsilon^2$, where $\sum_P$ represents the Pedersen conductance of the ionosphere. In fact, energy coupling is much more complicated than simple Joule heating leads to the formation of stormtime wind systems (**Richmond and Thayer, 2000**) that drive disturbance dynamos (**Blanc and Richmond, 1980**). Disturbance dynamos in turn alter prevailing electric field patterns throughout the MIT system. Many aspects of this high-to-low latitude electrodynamic coupling are now captured in computer simulations (**Maruyama et al., 2005**).

Energy enters the stormtime ionosphere at auroral and polar cap latitudes in the form of particle precipitation and Poynting flux (**Knipp et al., 2005**) and is mostly transferred to the thermosphere via ion-neutral collisions. Consequent heating of neutrals alters thermospheric scale heights allowing molecular species access to higher than quiet-time altitudes and generates winds that transport energy to subauroral latitudes. Quantitative understanding of how energy transport via neutral winds still has significant gaps. **Bruinsma and Forbes (2007)** identified a sequence of traveling atmospheric disturbances (TADs) in mid-to-low latitude measurements by the accelerometer on the Challenging Minisatellite Payload (CHAMP) satellite during a magnetic storm with multiple heat injections. Molecular scale heights, altered during TAD encounters, produce effects that are identifiable through remote-sensing techniques. **Lin et al. (2005)** showed that during the October–November 2003 superstorm both the $[O]/[N_2]$ ratios and total electron content (TEC) of the equatorial ionization anomaly decrease. The latter reflects enhanced recombination rates due to increased molecular concentrations in the F layer.

This report extends our preliminary study of IT responses observed by accelerometers on the Gravity Recovery and Climate Experiment (GRACE) satellites during the magnetic storms of November 2004. **Burke et al. (2007a)** found that:

(1) Presently used models under-predict stormtime density increases by >100%.
(2) Local densities ρ varied widely but global averages $\tilde{\rho}$ evolved systematically.
(3) Satellites crossing the polar cap near the noon–midnight meridian during magnetic storms experience positive and negative "density" spikes. These spikes are head- and tail-wind effects due to coupling with anti-sunward convecting ions.

* Correspondence to: AFRL/RVBXP, 29 Randolph Road, Hanscom AFB, MA 01731-3010, USA. Tel.: +1781 377 1312; fax: +1781 377 9950.
E-mail address: afrl.rvb.pa@hanscom.af.mil (C.Y. Huang).

1364-6826/$ - see front matter Published by Elsevier Ltd.
doi:10.1016/j.jastp.2009.06.005

(4) Magnetospheric electric fields $\varepsilon_{VS} \approx \Phi_{PC}/2L_\gamma R_E$ predicted from parameters observed at L_1 anticipate variations of $\bar{\rho}$ with lead times of 4–5 h. Φ_{PC} and $2L_\gamma R_E$ are the polar cap potential and width of the magnetosphere, respectively.
(5) During the main and early recovery phases $\bar{\rho}$ correlates with Dst.
(6) The thermosphere relaxes to pre-storm values much faster than Dst.

Allowing for local turbulence, result (2) suggests that on a global scale, the stormtime thermosphere evolves as a large thermodynamic system that never strays far from diffusive equilibrium (Wilson et al., 2006; Burke, 2008). The present analysis suggests that the stormtime thermosphere responds to interplanetary forcing as a driven-dissipative system whose dynamics are described by a simple differential equation.

In this paper, we compare global estimates of IT energy budgets during the magnetic storm of November 2004. Calculations employ three independent approaches. The first, involves calculating net (incident–reflected) Poynting flux ($S_\parallel$) into the ionosphere using electric ($\delta\varepsilon$) and magnetic ($\delta\mathbf{B}$) field perturbations measured along trajectories of Defense Meteorological Satellite Program (DMSP) spacecraft (Huang and Burke, 2004). The second, a statistical model developed by Weimer (2005) (W5), predicts distributions of $S_\parallel$ into the northern and southern high-latitude ionospheres using the solar wind (SW) and interplanetary magnetic field (IMF) as drivers. The third method uses orbit-averaged densities ($\bar{\rho}$) inferred from accelerometer measurements on the polar-orbiting GRACE satellites to estimate thermospheric energy (E_{th}) content at altitudes above 100 km (Burke, 2008). The following sections: (1) describe the methodologies and data sources, (2) provide examples of energy and power budgets during the November 2004 magnetic storm via the three different methods, and (3) comment on some implications of resultant similarities and differences.

2. Methodologies and data sources

The first method estimates $S_\parallel$ from drift meter and magnetometer measurements acquired along the trajectories of DMSP spacecraft as they cross the high-latitude ionosphere at 840 km. Using a transmission line analogy, Huang and Burke (2004) demonstrated that $S_\parallel \approx (\delta\varepsilon_\gamma \times \delta\mathbf{B}_Z)/\mu_0$ is the net (incident–reflected) Poynting flux. In making such calculations no knowledge about the distribution of conductivity beneath the spacecraft is required. Baselines for electric and magnetic-field calculations are established using the offset-subtraction technique described by Rich et al. (2007). Because it would be necessary to approximate energy depositions far from spacecraft trajectories, this is not a practical tool for making realistic estimates of total power/energy inputs to the global IT system. However, having direct measures of the actual electromagnetic energy inputs along trajectory lines provides quantitative means for evaluating and perhaps improving the predictions of global models such as W5 or AMIE.

Weimer (2005) combined two statistical models, initially developed to estimate the distributions of electric potential $\Phi(\Lambda, \phi)$ (Weimer, 1995) and field-aligned currents $j_\parallel(\Lambda, \phi)$ (Weimer, 2001) in the high-latitude ionosphere, to determine $S_\parallel$ as a function of magnetic latitude Λ, magnetic local time ϕ as well as the interplanetary magnetic-field magnitude and orientation. Maps of Poynting flux ($S_\parallel$), produced at 5 min intervals, reflect evolving solar-wind and IMF conditions. Total input power (P_{WS}) is determined by integrating $S_\parallel$ over affected areas of the ionosphere. Applying the first law of thermodynamics, Wilson et al. (2006) tested W5 by comparing quiet-time mass densities inferred from the drag exerted on 75 reference satellites at altitudes between 200 and 800 km (Casali et al., 2002; Storz et al., 2002) with their disturbed-time counterparts. Increased densities observed during periods of high magnetic activity were attributed to increases in the thermal energy content of the thermosphere and work done against the force of gravity. Energy increases inferred from the reference satellite data were similar to but less than predictions of W5. Since some of fraction of the energy must be deposited at altitudes below 200 km, these differences were regarded as being consistent with the model's general correctness.

The third approach uses orbit-averaged mass densities $\bar{\rho}$ measured by accelerometers on the polar-orbiting GRACE satellites (Tapley et al., 2004) to infer the total energy E_{th} of the thermosphere at altitudes $h > 100$ km. Because the technique is relatively new, a fuller explanation is required. As indicated in Fig. 1 the Jacchia model (Jacchia, 1977) (J77) consists of three elements. The first is a set of empirically based driving equations that relate variation of solar fluxes and the ap index to distributions of exospheric temperatures T_∞ (Bowman et al., 2006). The second consists of 15 tables that describe the thermospheric density and temperature T profiles required for diffusive equilibrium with given values of T_∞. The tables list profiles for $700 \le T_\infty \le 2000$ K in 100 K increments. The third element consists of predicted densities and consequent atmospheric drag exerted on space objects.

Burke (2008) argued that since T_∞ uniquely specifies each ρ–T–h profile in Jacchia tables and GRACE measures ρ at known altitudes, it should be possible to drive the model directly by accelerometer measurements. Treating table elements of the J77 model as though they were "real data," statistical analyses revealed that to a good approximation

$$T_\infty = \sum_{i=0}^{2} a_i(h)\rho^i(h) \tag{1}$$

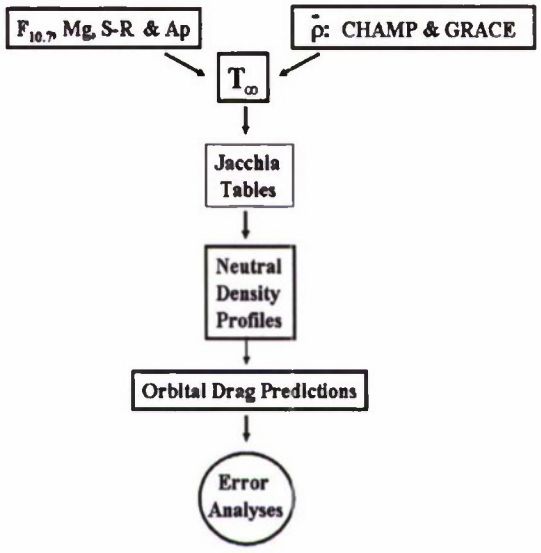

Fig. 1. Flow chart contrasting standard procedures (left) for estimating the atmospheric drag exerted on objects flying in low Earth orbit from observed solar UV radiances, and the ap index with a new method (right) using orbit-averaged mass densities inferred from measurements of accelerometers on the polar-orbiting CHAMP and GRACE satellites.

Over the range $300 < h < 500$ km each coefficient $a_i(h)$ is well represented by a fifth-order polynomial in h.

$$\begin{pmatrix} a_0(h) \\ a_1(h) \\ a_2(h) \end{pmatrix} = \begin{pmatrix} -28.10 & 2.69 & -2.03\times10^{-3} & 0 & 0 & 0 \\ -4.733\times10^{17} & 4.312\times10^{15} & -1.372\times10^{13} & 1.60\times10^{10} & 0 & 0 \\ 3.2695\times10^{32} & -4.620\times10^{30} & 2.618\times10^{28} & -7.456\times10^{25} & 1.071\times10^{23} & -6.237\times10^{19} \end{pmatrix} \times \begin{pmatrix} 1 \\ h \\ h^2 \\ h^3 \\ h^4 \\ h^5 \end{pmatrix} \quad (2)$$

Regression coefficients obtained in fitting T_∞ and a_i to polynomials exceed 0.999. In applying Eqs. (1) and (2) $\bar{\rho}$ and h are in grams/cc and kilometers, respectively. During the period of interest the orbit-averaged altitude of GRACE was ~486.7 km.

Using information contained within J77 tables and following the method of **Wilson et al. (2006)**, **Burke (2008)** demonstrated that the total (thermal and gravitational) energy of the thermosphere, in Joules, at $h > 100$ km is linearly related to the globally averaged exospheric temperature $\bar{T}_\infty$

$$E_{th}(J) = 5.365\times10^{17} + 8.727\times10^{13}\bar{T}_\infty \quad (3)$$

Over the T_∞ range 700–2000 K, E_{th} only changes by ~15%. Experience gained analyzing three years of data from the CHAMP and GRACE satellites indicates that during most storms $\bar{T}_\infty$ increased by a few hundred K. In comparison to base lines that reflect prevailing solar ultraviolet (UV) driving, stormtime percentage increases of E_{th} are small.

Burke (2008) noted two other relevant properties of the $\bar{\rho}$, $\bar{T}_\infty$, E_{th} triad: (1) they vary on time scales of solar rotations and geomagnetic activity represented by ε_{VS} and the Dst index. (2) Because they are related linearly, E_{th} and $\bar{T}_\infty$ decrease at the same rates whenever ε_{VS} turned off. Plots of $\ln E_{th}$ versus time (not shown) during magnetic storms indicate that as $\varepsilon_{VS} \to 0$, E_{th} relaxes with an e-fold time $\tau \approx 6.5$ h. The first property allows us to treat E_{th} as derived from two independent but additive sources, solar ultraviolet radiation $E_{th\ UV}$ and the solar wind $E_{th\ SW}$. As indicated below, the second property allows us to use time histories of ε_{VS} to estimate $E_{th\ SW}$ and then to compare its temporal variations with those determined from GRACE measurements of $\bar{\rho}$ with power input predictions of W5.

2.1. Data sources

The solar-wind density and velocity were measured by the solar wind electron, proton, and alpha monitor (SWEPAM) (**McComas et al., 1998**) and the IMF vector was observed by the magnetic-field instrument (MFI) (**Smith et al., 1998**) on the Advanced Composition Explorer (ACE) spacecraft in a halo orbit around L_1, ~234 R_E upstream of Earth.

Electric and magnetic-field perturbations were measured by ion drift meters (IDM) and triaxial fluxgate magnetometers on DMSP F13, F15, and F16. DMSP spacecrafts are three-axis stabilized and fly in circular, sun-synchronous, polar (inclination 98.7°) orbits at an altitude of ~840 km. The geographic local times of the orbital planes are near the 18:00–06:00 (F13), 20:00–08:00 (F16), and 2100–0900 (F15) LT meridians. Offsets between the geographic and geomagnetic poles allow DMSP spacecraft to sample wide ranges of magnetic local times over the course of a day. Each satellite carries a suite of sensors that measures the densities, temperatures, and drift motions of ionospheric ions and electrons (Special Sensor for Ions Electrons and Scintillations, SSIES), and perturbations of the Earth's magnetic field (Special Sensor for Magnetic Fields, SSM).

SSIES consists of spherical Langmuir probes on 0.8 m booms to measure electron densities and temperatures and three different sensors mounted on a conducting plate facing the satellite ram direction. They are: (1) an ion trap to measure the total ion densities; (2) an IDM to measure horizontal (V_H) and vertical (V_V) cross-track components of plasma drifts; (3) a retarding potential analyzer (RPA) to measure ion temperatures and the in-track component of plasma drift $V_\parallel$ (**Rich and Hairston, 1994**). Relatively small uncertainties about prevailing spacecraft potentials lead to unacceptable errors in $V_\parallel$ calculations and are not included in this study. Thus, Poynting fluxes calculated from DMSP measurements are lower-bound estimates. V_H and V_V are sampled 6 times per second but are normally reported as 4 s averages. They are then used to calculate the in-track component of electric field (ε_Y) and the distribution of electric potential (Φ) along the trajectory. DMSP estimates of the polar cap potential (Φ_{PC}) are reported as differences between measured potential extrema in the northern and southern hemispheres. Since trajectories usually do not cross potential maxima and minima, we also regard DMSP as providing lower-bound estimates of the true Φ_{PC}.

The triaxial fluxgate SSM sensors are either mounted on the spacecraft body (F13) or on 5 m booms (F15, F16) to reduce susceptibility to spacecraft-generated contamination. Magnetic vectors are sampled $16\,s^{-1}$ and reported as 1 s averages of $\delta\mathbf{B} = \mathbf{B}_{meas} - \mathbf{B}_{IGRF}$, differences between measured and International Geomagnetic Reference Field (IGRF) values of magnetic fields at the spacecraft locations. Data are presented as δB_X, δB_Y, δB_Z in a spacecraft-centered coordinate system. The X- and Y-axis point toward spacecraft nadir and along its velocity vector, respectively. The Z-axis completes the right-hand system and generally points in the anti-sunward direction. The downward component of Poynting flux is estimated as $S_\parallel \approx (\delta\varepsilon_Y \times \delta\mathbf{B}_Z)/\mu_0$. Values of $S_\parallel$ presented below were calculated and reported at a cadence of one sample per second.

Neutral densities at ~486.7 km were estimated from measurements of Spatial Triaxial Accelerometer for Research (STAR) sensors on two GRACE satellites flying in tandem in nearly circular, polar orbits (**Tapley et al., 2004**). STAR sensors monitor electrostatic forces needed to maintain proof masses (PM) at the center of a cage located within 2 mm of each spacecraft's center of mass (**Bruinsma et al., 2004**). Both the spacecraft and PM respond to gravity in the same way. Thus, changes in electrostatic forces that maintain the PM at its cage's center reflect spacecraft responses to non-gravitational forces such as atmospheric drag and radiation pressure (**Bruinsma and Biancale, 2003**). Acceleration due to drag is given by

$$a_{drag} = C_D A_{sc}/2M_{sc}\rho V^2 \quad (4)$$

where A_{sc} and M_{sc} represent the effective cross-sectional area and mass of the spacecraft, respectively, ρ the mass density of the neutral atmosphere, and V the spacecraft velocity in the rest frame of ambient neutrals. The drag coefficient C_D depends on the angle of flow to the spacecraft surface, the ratio of the temperatures of the satellite surface and the local atmosphere, and the ratio of the

mean mass of atoms in the atmosphere to those on the satellite surface (Bruinsma and Biancale, 2003).

3. Observations

This report focuses on electrodynamic responses observed on November 10, 2004. Here, we refer to both calendar dates and Julian days (JD) of the year, where January 1 corresponds to JD 1. Reported events of JD 315 occurred within a larger disturbance. Fig. 2 provides context in the form of the Dst index (top), the ring-current energy E_{RC} (middle), and ε_{VS} (bottom) for JD 310–316 (November 5–11). E_{RC} was calculated using a form of the DPS theorem given by Stern (2005): $E_{RC} \approx (3\ \mathrm{Dst}\ E_M/2B_0)$, where $B_0 \approx 3.1 \times 10^4$ nT is the magnetic field at the equator, and $E_M \approx 8 \times 10^{17}$ J the magnetic-field energy above the Earth's surface. Methods used to calculate ε_{VS} are described in Appendix A.

Plots in Fig. 2 show that the disturbance began late on JD 312 (November 7) after a long quiet period. The first main phase reached a maximum epoch at 06:00 UT on JD 313 (November 8) when Dst and E_{RC} reached −372 nT and $\sim 1.5 \times 10^{16}$ J, respectively. Figures 3d and 4d of Burke et al. (2007b) show that the quantity $I_{VS} = \int \varepsilon_{VS}(t)\,dt$ highly correlates with Dst during the main-phase episode of JD 313. Magnetic quieting was interrupted late on JD 314 by a brief, but intense, southward turning of the IMF that led to a spike in ε_{VS} of ~2.3 mV/m near 19:00 UT. The geomagnetic disturbance resumed on JD 315 with Dst reaching a minimum of −289 nT ($E_{RC} \approx 1.2 \times 10^{16}$ J) at 09:00 UT.

Plots in Fig. 3 show thermospheric responses as observed by GRACE in polar orbit near the noon–midnight meridian. The figure shows orbit-averaged densities (top), exospheric temperatures

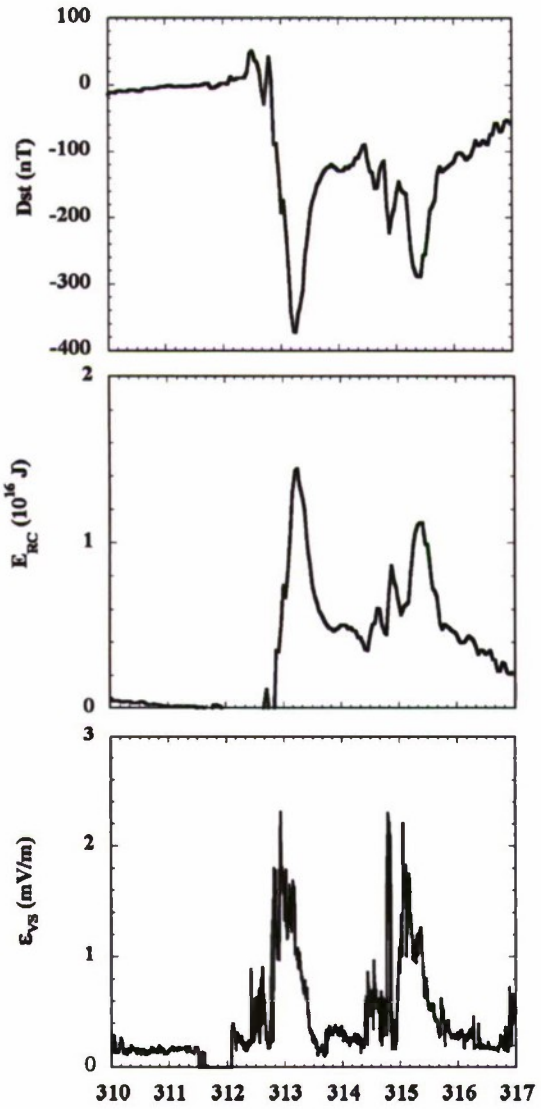

Fig. 2. History of the Dst index (top) from November 5–11, 2004 (Julian days 310–316), the energy of the ring-current E_{RC} estimated via the Dessler–Parker–Sckopke relation (middle) and the Volland–Stern electric field ε_{VS} determined from ACE measurements near L_1 (bottom) plotted as functions of UT.

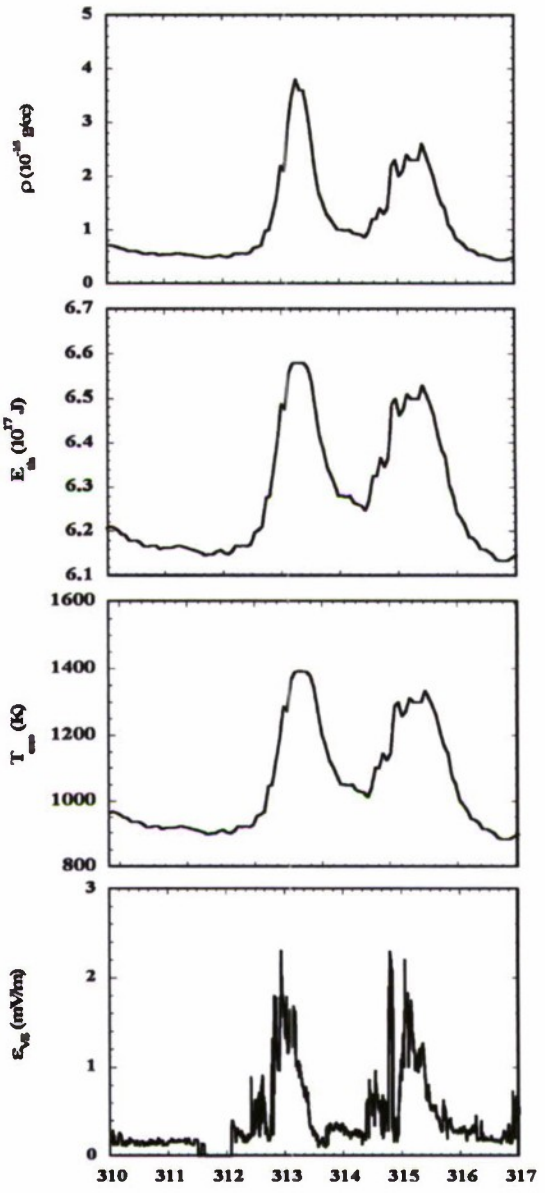

Fig. 3. GRACE measurements of orbit-averaged mass densities (top), exospheric temperatures (second), and thermospheric energy (third) plotted as functions of UT for (November 6–14) 310–317 (November 6–14), 2004. The ε_{VS} trace is repeated for reference in the bottom panel.

(second), total thermospheric energies, and ε_{VS} (bottom) plotted as functions of time over the same 7-day interval as in Fig. 2. $\bar{T}_e$ and E_{th} were calculated using Eqs. (1) and (3), respectively. Attention is directed to six empirical features apparent in the data:

(1) Decreasing trends in traces of $\bar{\rho}$, $\bar{T}_e$, and E_{th} on JD 310 and 311 when ε_{VS} was small are solar rotation effects indicated by a decreasing $F_{10.7}$ (not shown).
(2) At the beginning of JD 312, $\bar{T}_e$ and E_{th} were ~925 K and 6.15×0^{17} J, respectively.
(3) $\bar{T}_e$ and E_{th} maxima reached ~1400 K and 6.6×10^{17} J, respectively on JD 313.
(4) E_{th} increased by 5.5×10^{16}, while E_{RC} only reached 1.2×10^{16} on JD 315.
(5) $\bar{T}_e$ and E_{th} attained maxima of ~1350 K and 6.55×10^{17} J, respectively on JD 315.
(6) $\bar{T}_e$ and E_{th} fell at the same rate on JD 313 and 315 after ε_{VS} turned off.

Fig. 4 illustrates the procedure used for comparing W5 predictions of $S_\parallel$ with DMSP measurements. The left plot shows a typical W5 Poynting flux map on a $(\Lambda-\phi)$ grid. Iso-contour lines indicate the spatial distribution of electromagnetic power into the southern hemisphere near the end of the main phase (09:45 UT) of the November 10 disturbance. The W5 map shows two local maxima in $S_\parallel$ at stormtime auroral latitudes of 58° and 62° MLat near dusk and dawn, respectively. Significant but lesser power flows into the polar ionosphere. Curiously, the model assigns almost no electromagnetic power input to the regions of the dayside cusp or the midnight sector of the auroral oval. Indicated to the lower left and right of the map are magnitudes of minimum and maximum $S_\parallel$. Integrated power into the southern polar cap (886 GW) is provided in the upper right corner. The solid orange line across the contour map indicates the dawn-to-dusk trajectory of DMSP F13 across the southern polar cap at about the same UT. The trajectory passed through the predicted morning side maximum, but missed the one on the evening side. The plot on the right side of Fig. 4 compares W5 Poynting flux predictions along the F13 orbit with data from combined IDM and SSM measurements. With obvious *caveats*, this instance shows reasonable agreement between W5 predictions and DMSP observations. However, most W5 and DMSP $S_\parallel$ distributions do not agree so closely. We note that as F15 crossed the southern auroral oval at ~10:03 UT it recorded peak $S_\parallel$ values of ~40 mW/m^2 near MLat = −57°, MLT = 23.0, where the W5 map assigns very little Poynting flux.

To support quantitative comparisons between the thermospheric power inputs predicted by W5 and measured by DMSP, without becoming bogged down with local variations, we decided to compare two global parameters. W5 routinely calculates power into the northern and southern ionospheres every 5 min. We add these together to obtain the predicted global P_{WS}. We also integrated $S_\parallel$ (W/m) measurements along full trajectories of DMSP F15 and F16 to calculate a quantity

$$\Pi_\parallel(W/m) = \oint S_\parallel \, ds = V_{sat} \int S_\parallel \, dt \approx 7.5 \times 10^3 \sum_{n_i}^{n_f} (\delta E_Y \times \delta B_Z)_i / \mu_0 \tag{5}$$

The absence of $(\delta E_Z \times \delta B_Y)_i/\mu_0$ from $S_\parallel$ in Eq. (5) reflects our inability to extract reliable estimates of the in-track component of plasma drift from current–voltage sweeps of retarding potential analyzers on DMSP satellites (**Rich and Hairston, 1994**). Integrals/sums extend from one ascending or descending node to the next and are reported at the times of the second equatorial crossing. The top panel of Fig. 5 contains results of $S_\parallel$ calculations for DMSP F15 (diamonds) and F16 (circles) on November 9 and 10. The plot in the middle shows the history of global power input predicted by W5. For reference ε_{VS} is shown at the bottom. Data presented in Fig. 5 support three empirical conclusions:

(1) Agreement between F15 and F16 measurements of $S_\parallel$ was close on JD 314. While agreement remained good on JD 315, the correlation clearly degenerated. This is primarily a spatial effect. On both days the separation of ascending nodes for the two spacecraft was ~3 min in UT and ~1 h in LT. A linear correlation analysis (not shown) indicates that $\prod_{\parallel F15} = 1.85 + 0.91 \prod_{\parallel F16}$; the correlation coefficient is ~0.83. The < 1 slope agrees with the sense of W5 zonal gradients.
(2) While it is possible to establish correspondence between $\prod_\parallel$ structures and events in the P_{WS} trace, overall agreement does not appear strong.
(3) However, remarkable agreement is evident between P_{WS} and ε_{VS} features.

We comment on the significance of the 2nd and 3rd observations in the discussion section.

While our emphasis has been on global-scale variations of thermospheric parameters, we recognize that this is not the whole

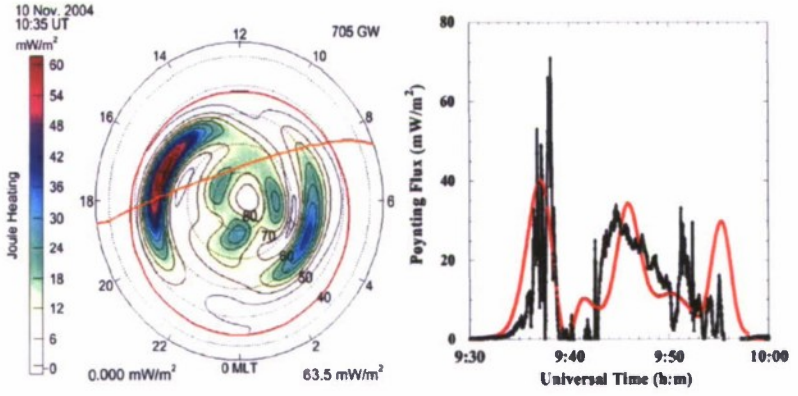

Fig. 4. Contours of Poynting flux $S_\parallel$ predicted by WS for the southern hemisphere at 09:45 UT on November 10, 2004 (left). The dawn-to-dusk trajectory of DMSP F13 is indicated by an orange line across the map. Plots on the right side compare F13 Poynting flux measurements (black) with WS predictions (red) along the F13 trajectory. (For interpretation of the references to colour in this figure legend, the reader is referred to the web version of this article.)

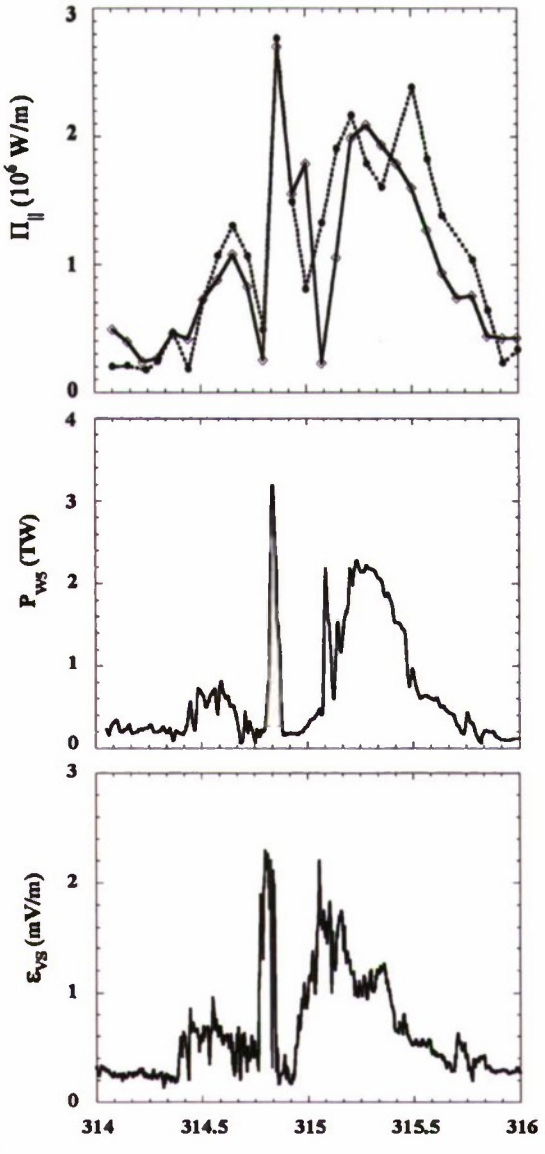

Fig. 5. Orbit-integrated Poynting flux $S_{\parallel}$ (top) measured by DMSP F15 (diamonds) and F16 (circles) and global power P_{WS} input predicted by W5 (middle), plotted as functions of UT for JD 314 and 315 (November 10–11), 2004. The ε_{VS} trace (bottom) is provided for comparison with P_{WS}.

story. Data shown in Fig. 6 illustrate some of the complex dynamics that dominate local measurements. The traces show neutral densities measured by GRACE during four successive nighttime orbital passes plotted as functions of geographic latitude. In November 2004, the satellite trajectory passed from north to south close to the midnight meridian. Thus, GRACE crossed the southern polar cap from night to day. Above the panels we indicate the universal times of equatorial crossings on November 10. During the first orbit GRACE detected a density maximum slightly north of the equator. Observed densities varied by a factor of ~2 across all nightside latitudes. In the second panel, labeled 02:50:02 UT, a large spike appears at high southern latitudes, that is in part a headwind effect (Burke et al., 2007a), while a broad featureless valley extended across the middle and low-latitude thermosphere. By the time of the equatorial crossing at 04:24:27 UT, three distinct density maxima were seen at latitudes extending from −80° to 60°. By the time of the 05:58:17 UT pass, the highest densities were once more found near the equator. Densities measured in these maxima are about three times larger than those observed at mid-to-high latitudes. We discuss possible connections between these observations and TADs reported by Bruinsma and Forbes (2007) in the following section.

4. Discussion

In the previous section, we applied a new method for estimating the thermosphere's total energy content E_{th} using orbital averages of densities inferred from measurements of accelerometers on the polar-orbiting GRACE satellites. Data were also provided that allow comparisons (1) between the estimated E_{th} and E_{RC} during the November 2004 storm, and (2) with thermospheric energy and power requirements inferred from GRACE measurements and W5, respectively. Based on these comparisons and simultaneous DMSP measurements of $S_{\parallel}$, we comment on the Poynting flux distributions of the W5 model. Finally, we briefly discuss the mutually supportive roles of *in situ* measurements from GRACE and information gained through remote sensing of $[O]/[N_2]$ ratios and the TEC content of the low-latitude ionosphere.

Huang and Burke (2004) reported repeated episodes of intense Poynting flux infusions to the auroral oval during the main phase of large magnetic storms. Four DMSP satellites detected these phenomena over a wide range of nightside local times. This observed spatial distribution suggested that energy transferred to the magnetosphere from the enhanced solar wind largely accumulates in the ring current. The ring current would thus function as a reservoir from which particle and electromagnetic energy is drawn to heat the stormtime IT system. The W5 map in Fig. 4 appears compatible with this perception, placing most $S_{\parallel}$ to the ionosphere at auroral rather than polar cap latitudes.

If this conjecture is correct, we expect that E_{RC} would exceed stormtime increases in E_{th}, perhaps by large amounts. Calculations plotted in Figs. 2 and 3 indicate the opposite is true, $\Delta E_{th} \approx 3$ E_{RC}. A similar relation was found during the magnetic storms of July 2004 (Burke, 2008). The DPS theorem thus indicates that the ring current cannot act as a reservoir for most of the energy reaching the stormtime thermosphere as suggested by Huang and Burke (2004). Magnitudes of Φ_{PC} calculated from ACE data (cf. Appendix A) and observed by DMSP were >200 kV on both November 8 and 10, 2004. To supply the entire peak power of ~2–3 TW predicted by W5 (Fig. 5) on JD 315, Pedersen currents of ~5 MA would have to flow across both polar caps. Since some significant fraction of the total power must enter the *I–T* at auroral latitudes, actual trans-polar current demands are correspondingly less than the 5 MA estimate.

To make meaningful comparisons between the W5 predictions and GRACE measurements it is critical to recognize fundamental differences between them. W5 uses solar-wind/IMF measurements to predict distributions of Poynting flux into the northern and southern ionospheres. Integration over the affected areas provides the global rates of energy input. On the other hand, orbit-averaged E_{th} measurements from GRACE are snapshots that capture the total energy content of the thermosphere during a given interval of time. They reflect thermospheric give and take between power received from the outside and lost via radiative and other processes (Mlynczak et al., 2005).

We noted above that E_{th} varies on time scales that correspond to the solar rotation period and changes in ε_{VS} (Burke, 2008). We have found that as $\varepsilon_{VS} \rightarrow 0$, $E_{th\ SW}$ relaxes with an e-fold time scale of $\tau \approx 6.5$ h. This behavior suggests that the global thermosphere

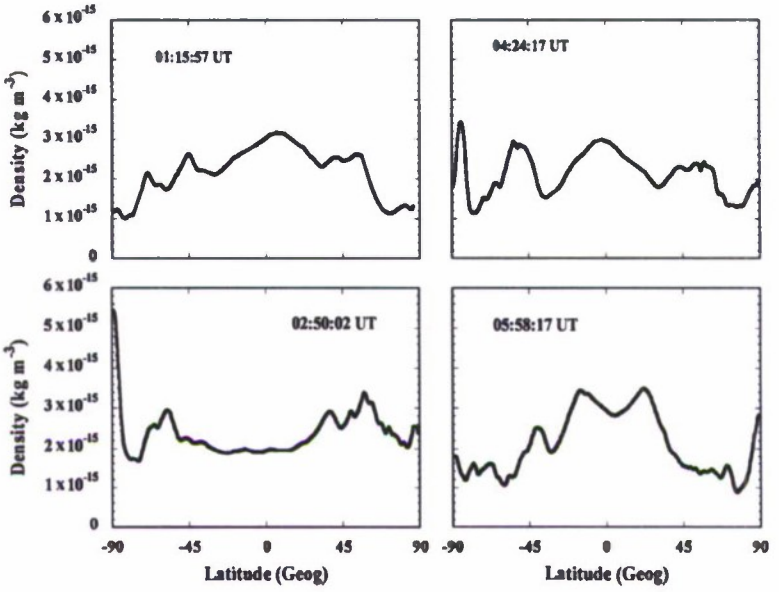

Fig. 6. Thermospheric mass densities measured by GRACE during four consecutive passes on November 10, 2004 along the midnight meridian plotted as functions of latitude. The universal times of corresponding equatorial crossings are noted above the plots.

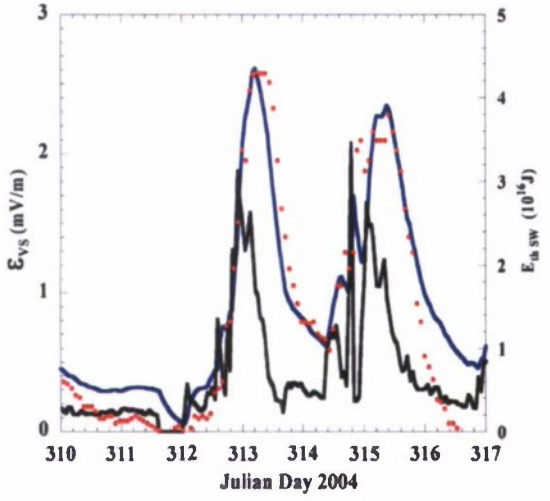

Fig. 7. Plots of ε_{VS} (black line) and values of $E_{th\ SW}$ predicted by Eq. (5) (blue line) and measured by GRACE (red dots). (For interpretation of the references to colour in this figure legend, the reader is referred to the web version of this article.)

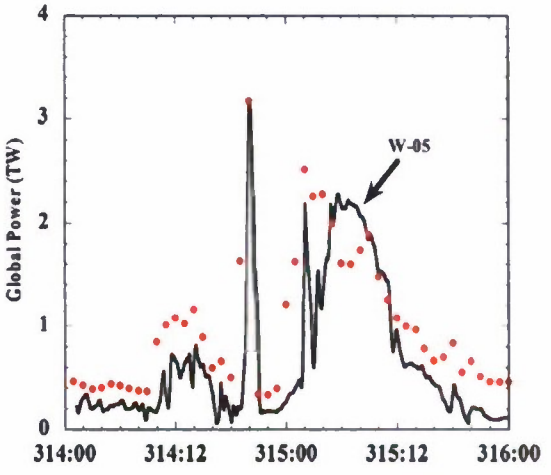

Fig. 8. Comparison of $\alpha\varepsilon_{VS}$ required by Eq. (6) to match GRACE measurements of E_{th} with P_{WS} inputs predicted for November 9 and 10, 2004.

acts as a driven-dissipative system. The well-known differential equation describing energy changes in such systems has the form

$$\frac{dE_{th\,SW}}{dt} = \alpha\varepsilon_{VS} - \frac{E_{th\,SW}}{\tau} \tag{6}$$

Similar equations govern the evolution of energy in R-L circuits and the ring current during magnetic storms (Burton et al., 1975). Coupling and relaxation constants α and τ must be determined empirically. Eq. (6) is solved numerically by

$$E_{th\,SW}(t_{n+1}) = \alpha\varepsilon_{VS}(t_n)\Delta t + E_{th\,SW}(t_n)\left(1 - \frac{\Delta t}{\tau}\right) \tag{7}$$

Using solar-wind and IMF measurements from the ACE satellite we calculated hourly averages of ε_{VS}. For convenience we take the time interval Δt to be 1 h. A preliminary analysis of GRACE and ε_{VS} measurements indicates that if we consider E_{th} in units of 10^{16} J, the coupling constant $\alpha \approx 0.55$. Fig. 7 compares predictions of Eq. (7) (blue line) with values of $E_{th\ SW}$ inferred from GRACE accelerometer measurements (red dots) during the November storm period. The black line repeats the history of the ε_{VS} driver. Although we have not tried to optimize estimates of α and τ, agreement between predictions and measurements appears to be close.

Eq. (6) calculates the net power into the thermosphere as power input ($\alpha\varepsilon_{VS}$) minus the dissipation ($E_{th\ SW}/\tau$). Thus, $\alpha\varepsilon_{VS}$ represents the power input needed to replicate GRACE measurements and should be directly comparable with P_{WS}. If we represent E_{th} in Joules, $\alpha \approx 5.5 \times 10^{15}$((J/h)/(mV/m)) = 1.528 TW/(mV/m). The black trace in Fig. 8 replicates the middle panel of Fig. 5, showing net power P_{WS} TW; red dots indicate corresponding values of $\alpha\varepsilon_{VS}$ time-shifted by 1 h to allow for transport from L_1 to the magnetosphere. Correspondence between

P_{WS} and $\alpha\varepsilon_{VS}$ appears close. Both methods indicate that at several times peak power inputs reached the 2–3 TW range. This significantly exceeds ~500 GW of power incident to the dayside of Earth at EUV wavelengths (Knipp et al., 2005). Agreement between P_{WS} and $\alpha\varepsilon_{VS}$ independently confirms the J77 analysis of GRACE measurements and indicates that P_{WS} can be used to drive Eq. (6) to predict the development calculations of $E_{th\ SW}$ and $\hat{T}_{e,i}$.

Siscoe (1983) demonstrated that only "obliquely propagating" Alfvén waves carry field-aligned current. These waves also carry field-aligned Poynting flux from regions where $\nabla \cdot S > 0$. Both $J_\parallel$ and $S_\parallel$ propagate along field lines that, in an Earth stationary frame of reference, move in the $\mathbf{V_D} = (\mathbf{E_C} \times \mathbf{B})/B^2$ direction, where $\mathbf{E_C}$ represents the background convection electric field. Strictly speaking, at ionospheric altitudes the field line is not exactly conjugate to the $J_\parallel$ and $S_\parallel$ source locations. However, they can only be removed from the source location by a distance $\mathbf{V_D} \cdot \Delta T_A$. Here, ΔT_A is the Alfvén travel time required for the signal to propagate from the magnetospheric source to the ionosphere. At typical plasma sheet and ring-current distances the separations are relatively small. Data in Fig. 4 place the bulk of $S_\parallel$ predicted by W5 at auroral latitudes. As such $S_\parallel$ sources appear to lie in the plasma sheet and ring current. Data presented in Figs. 2 and 3 demonstrate that $E_{th\ SW} \approx 3E_{RC}$. Given the hour-long time scales needed to transport and energize ring-current particles, it is difficult to understand how energy would be processed in the magnetosphere in ways that explain the observed high and sustained rates of power transported to the stormtime auroral ionosphere–thermosphere. Resolution to this apparent discrepancy lies in the fact that the peak magnitude of $S_\parallel$ is located at the boundary between Regions 1 and 2 currents. The dividing line between the solar-wind and ring-current sources of Poynting flux lies somewhat poleward of the peak, but still within the auroral oval. It is possible that an area integration of $S_\parallel$ within different regions will confirm the three to one ratio, but this calculation is beyond the scope of this observational report.

A comparison with the Dst trace in Fig. 2 shows that latitudinal density profiles in Fig. 6 were acquired as magnetic activity emerged from a 6 h lull (314:22 to 315:04 UT) into the main-phase intensification. The intensities of peak latitudinal variations observed near 04:24 and 05:58 UT exceeded those of troughs by >50%. We tentatively interpret these structures as signatures of equatorward propagating TADs similar to those reported by Bruinsma and Forbes (2007).

TADs provide evidence of energy transport from the auroral zones where heating occurs towards the equator where the atmospheric pressure is lower. However, the Earth rotates by ~23° in longitude from one ascending-node crossing of GRACE's orbit to the next. To interpret the structures such as those detected by GRACE (Fig. 6) as TADs, it is necessary to assume that they extend over wide swaths of longitude (Bruinsma and Forbes, 2007). Here, information gained through remote-sensing techniques is supportive. Because of their effects on $[O]/[N_2]$ ratios and TEC at low latitudes, TAD effects can be associated with Composition Perturbation Zones (CPZ) (Lin et al., 2005). During the same interval as the data shown in Fig. 6, Hei (private communication, 2008) observed TEC decreases that progressed from high latitudes in the southern (summer) hemisphere toward the equator. Critical for the interpretation of structures detected by accelerometers, Hei and coworkers determined from UV images that CPZs do indeed maintain coherence over several hours in local time (longitude).

5. Summary and conclusions

In this paper, we employed three independent techniques to estimate the amount of energy that entered the high-latitude ionosphere–thermosphere as Poynting flux during the magnetic storm of November 2004. (1) Data from plasma drift and magnetic-field sensors on the DMSP F15 and F16 spacecraft combine to support calculations of Poynting flux along trajectories. (2) The empirical model of Weimer (2005) uses plasma and magnetic-field measurements acquired near L_1 to predict Poynting flux distributions in magnetic latitude and magnetic local time at a 5-min cadence. Total power P_{WS} input is obtained by integrating over the affected area of the upper atmosphere. (3) We introduced a new technique that uses orbit-averaged mass densities measured by the polar-orbiting GRACE satellites to infer E_{th} the total energy content of the thermosphere. Values of E_{th} above quiet-time levels were compared with E_{RC} the energy content of the ring current estimated via the Dessler–Parker–Sckopke relation. Observed properties of E_{th} responses to ε_{VS} driving indicate that the global thermosphere acts as a driven-dissipative system whose behavior is described by a simple first-order differential equation. The coupling (α) and relaxation (τ) constants of the equation were established empirically through comparisons with GRACE data. An independent test compared the histories of power inputs $\alpha\varepsilon_{VS}$ required to explain measurements with those of P_{WS}. Comparison results (Fig. 8) are in excellent agreement.

Unlike solar EUV radiation that most strongly heats the thermosphere at low-to-mid latitudes, stormtime energy inputs occur in the auroral oval and polar cap. Nonetheless, distinctive signatures of stormtime disturbances appear at subauroral latitudes. These include diminished TEC and $[O]/[N_2]$ ratios that indicate some of the stormtime energy input is transported away from high-latitude sources. GRACE measures of mass density profiles along the midnight meridian (Fig. 6) illustrate the equatorward propagation of thermospheric structures that reach the equator ~3 h after energy injection at high latitudes.

The four main conclusions of our analysis of the November 10, 2004 magnetic storm are:

1. Although Poynting flux distributions from DMSP and W5 predictions sometimes agree (Fig. 4), this is not always the case. Breakdown in agreement is most evident in the midnight sector of the auroral oval. Integrated values of Poynting flux measured by DMSP agree fairly well with W5 predictions.
2. Energy added to the stormtime thermosphere is ~3 E_{RC}. A large fraction of the peak energy of $\sim 4 \times 10^{16}$ J reached the thermosphere at magnetic latitudes that are not conjugate to the ring current.
3. Electromagnetic power into the thermosphere during the November 2004 storm, estimated as $\alpha\varepsilon_{VS}$ and P_{WS}, attained peak values of 2–3 TW and exceed the total EUV power to the entire dayside of the Earth (Knipp et al., 2005).
4. In agreement with dayside results of Bruinsma and Forbes (2007), it takes about 3 h after an energy injection for a TAD to reach the equator on the nightside.

Acknowledgments

Support for the presented work was provided by the Air Force Office of Scientific Research, Task 2301SDA5 and AF Contracts FA8718-04-C-0055 and FA8718-08-C-0012 with Boston College. We thank B. R. Tapley of the University of Texas for access to GRACE measurements.

Appendix A. : Volland–Stern (V–S) electric fields

As formulated by Ejiri (1978) the Volland–Stern model offers a simple, albeit limited, method for estimating the trajectories of

ring-current ions in the inner magnetosphere. One difficulty in applying the model relates to the connection between the interplanetary and magnetospheric electric fields. **Burke (2007)** reformulated V–S by combining it with the Siscoe–Hill (S–H) model of the polar cap potential (Φ_{PC}) to show that in the absence of shielding the electric field in the inner magnetosphere is $\varepsilon_{VS} \approx \Phi_{PC}/2R_E L_Y$, where the denominator represents the width of the magnetosphere along the dawn–dusk line. This appendix outlines our method for calculating ε_{VS} values used in the main text.

Empirical studies suggest that on the dayside the equatorial magnetopause is nearly self-similar in shape with $L_Y \approx 1.5\ L_X$ (**Roelof and Sibeck, 1993**). Force balance at the subsolar magnetopause requires that

$$L_X \approx \sqrt[6]{\frac{B_0^2}{\mu_0 P_{SW}}} \approx \frac{9.6}{\sqrt[6]{P_{SW}(\text{nPa})}} \text{ and } L_Y \approx 14.4/\sqrt[6]{P_{SW}(\text{nPa})} \quad \text{(A1)}$$

More precise estimates of magnetopause dimensions that include erosion effects can be introduced where more rigorous calculations are required.

Between 1980 and 2000 many investigators sought linear relationships between Φ_{PC} and interplanetary parameters (**Weimer, 1995**; **Boyle et al., 1997**). **Burke et al. (1999)** surveyed analyses of Φ_{PC} dependence on solar-wind parameters and showed that in the linear regime consistently high correlation coefficients were obtained with

$$\Phi_E(\text{kV}) = \Phi_0 + L_G V_{SW} B_T \sin^2 \frac{\theta}{2} \quad \text{(A2)}$$

The subscript E refers to interplanetary electric-field contributions; Φ_0 is a residual potential with typical values between 20 and 30 kV, $B_T = \sqrt{(B_Y^2 + B_Z^2)}$, and θ the IMF clock-angle in the GSM Y–Z plane. Because the clock-angle enters IEF calculations through the positive-definite quantity $\sin^2\theta/2$, we ignore quadrant distributions and approximate θ as $\cos^{-1}(B_Z/B_T)$. If we express $V_{SW}B_T$ in kV/R_E (where 1 mV/m $\approx$ 6.4 kV/R_E) then the regression slope L_G represents a 3–4 R_E wide "gate" in the solar wind through which geoeffective streamlines (equipotentials) must pass to reach the dayside magnetopause.

Siscoe et al. (2002) suggested that during large magnetic storms Region 1 currents generate perturbation magnetic fields that alter the shape of the dayside magnetopause, thereby limiting access of solar-wind streamlines and forcing the merging rate to saturate. Following the suggestion of **Hill (1984)**, **Siscoe et al. (2002)** postulated that a saturation potential Φ_S contributes to Φ_{PC}

$$\Phi_{PC} = \frac{\Phi_E \Phi_S}{\Phi_E + \Phi_S} \quad \text{(A3)}$$

Note that when $\Phi_E \ll \Phi_S$, $\Phi_{PC} \to \Phi_E$, and the standard linear relation Eq. (A2) is retrieved. **Siscoe et al. (2002)** derived an expression for Φ_S in kV

$$\Phi_S(\text{kV}) = \frac{1600\sqrt[3]{P_{SW}(\text{nPa})}}{\Sigma_P(\text{mho})} \quad \text{(A4)}$$

where P_{SW} is the dynamic pressure of the solar wind and $\sum_P$ the effective Pedersen conductance of the polar ionosphere. **Ober et al. (2003)** used data from the SWEPAM and MFI on ACE to compare Φ_{PC} predictions of S–H and other models with DMSP measurements during the magnetic storm of March 2001. Under pre-storm conditions all of the models predicted Φ_{PC} values measured by DMSP. During the main phase S–H predictions of Φ_{PC} provided an excellent, upper-bound envelope for DMSP observations. Linear models predicted much larger than observed Φ_{PC}. **Burke et al. (2007b)** found that setting $\sum_P = 10$ mho provided excellent agreement between calculated and observed Φ_{PC} during a large number of magnetic storms near both equinoxes and solstices.

In computations of ε_{VS} we used hourly averaged values of the solar-wind density and velocity from SWEPAM and IMF components in solar-magnetospheric coordinates from the MFI on ACE. In applications to S–H we set $\Phi_0 = 25$ kV, $L_G = 3.5$, and $\sum_P = 10$ mho.

References

Blanc, M., Richmond, A.D., 1980. The Ionospheric disturbance dynamo. J. Geophys. Res. 85, 1669.

Bowman, B.R., Tobiska, W.K., Marcos, F.A., 2006. A new empirical thermo-spheric density model JB2006 using new solar indices. AIAA Astrodynamics Conference, AIAA 2006–6166, Keystone, CO.

Boyle, C.B., Reiff, P.H., Hairston, M.R., 1997. Empirical polar cap potentials. J. Geophys. Res. 102(A), 111.

Bruinsma, S.L., Biancale, R., 2003. Total densities derived from accelerometer data. J. Spacecr. Rockets 40, 230.

Bruinsma, S.L., Tamagnan, D., Biancale, R., 2004. Atmospheric densities derived from CHAMP/STAR accelerometer observations. Planet. Space Sci. 52, 297.

Bruinsma, S.L., Forbes, J.M., 2007. Global observations of travelling atmospheric disturbances (TADs) in the thermosphere. Geophys. Res. Lett. 34, L14103.

Burke, W.J., 2007. Penetration electric fields: a Volland–Stern approach. J. Atmos. Sol.-Terr. Phys. 69, 1114.

Burke, W.J., 2008. Stormtime energy budgets of the global thermosphere. In: Kintner, P.M., Coster, A.J., Fuller-Rowell, T., Mannucci, A.J., Mendillo, M., Heelis, R.A. (Eds.), Mid-Latitude Ionospheric Dynamics and Disturbances. Washington, DC, pp. 235–246 (American Geophysical Monograph 181).

Burke, W.J., Weimer, D.R., Maynard, N.C., 1999. Geoeffective interplanetary scale sizes derived from regression analysis of polar cap potentials. J. Geophys. Res. 104, 9989.

Burke, W.J., Huang, C.Y., Marcos, F.A., Wise, J.O., 2007a. Interplanetary control of thermospheric densities during large magnetic storms. J. Atmos. Sol.-Terr. Phys. 69, 279.

Burke, W.J., Gentile, L.C., Huang, C.Y., 2007b. Penetration electric fields driving main-phase Dst. J. Geophys. Res. 112.

Burton, R.K., McPherron, R.L., Russell, C.T., 1975. An empirical relationship between interplanetary conditions and Dst. J. Geophys. Res. 80, 4204.

Carovillano, R.L., Siscoe, G.L., 1973. Energy and momentum theorems in magnetospheric processes. Rev. Geophys. 11, 289.

Casali, S.J., Barker, W.N., Storz, M.F., 2002. Dynamic calibration atmosphere (DCA) tool for the high accuracy satellite drag model (HASDM). AAS/AIAA Astrodynamics Specialist Conference, AIAA 2002–4888, Monterey, CA.

Ejiri, M., 1978. Trajectory traces of charged particles in the magnetosphere. J. Geophys. Res. 83, 4798.

Hill, T.W., 1984. Magnetic coupling between solar wind and magnetosphere: regulated by ionospheric conductance. EOS, Trans. Am. Geophys. Union 65, 1047.

Huang, C.Y., Burke, W.J., 2004. Transient sheets of field-aligned current observed by DMSP during the main phase of a magnetic storm. J. Geophys. Res. 109, A06303.

Jacchia, L.G., 1977. Thermospheric temperature, density, and compositinn: New models, SAO special report no. 375.

Knipp, D.J., Tobiska, W.K., Emery, B.A., 2005. Direct and indirect thermospheric heating sources for solar cycles 21–23. Sol. Phys. 224, 495.

Lin, C.H., Richmond, A.D., Liu, J.Y., Yeh, H.C., Paxton, L.J., Tsai, H.F., Su, S.-Y., 2005. Large-scale variations of the low latitude ionosphere during the October–November 2003 superstorm: observational results. J. Geophys. Res. 110, A09S28.

Maruyama, N., Richmond, A.D., Fuller-Rowell, T.J., Codrescu, M.V., Sazykin, S., Toffoletto, F.R., Spiro, R.W., Millward, G.H., 2005. Interaction between direct penetration and disturbance dynamo electric fields in the storm-time equatorial ionosphere. Geophys. Res. Lett. 32, L17105.

McComas, D.J., Bame, S.J., Barber, P., Fieldman, W.C., Phillips, J.L., Riley, P., 1998. Solar wind electron, proton, and alpha monitor (SWEPAM) on the advanced composition explorer. Space Sci. Rev. 86, 563.

Mlynczak, M.G., Martin-Torres, F.J., Crowley, G., Kratz, D.P., Funke, B., Lu, G., Lopez-Puertas, M., Russell, J.M., Kozyra, J., Mertens, C., Sharma, R., Gordley, L., Picard, R., Winick, J., Paxton, L., 2005. Energy transport in the thermosphere during the solar storms of April 2002. J. Geophys. Res. 110, A12S25 (doi:1029/2005JA011141).

Ober, D.M., Maynard, N.C., Burke, W.J., 2003. Testing the hill model of transpolar potential saturation. J. Geophys. Res. 108 (A12), 1467.

Rich, F.J., Hairston, M., 1994. Large-scale convection patterns observed by DMSP. J. Geophys. Res. 99, 3827.

Rich, F.J., Bono, J.M., Burke, W.J., Gentile, L.C., 2007. A proxy for the Dst index. J. Geophys. Res. 112, A05211.

Richmond, A.D., Kamide, Y., 1988. Mapping electrodynamic features of the high-latitude ionosphere from localized observations: technique. J. Geophys. Res. 93, 5741.

Richmond, A.D., Thayer, J.P., 2000. Ionospheric Electrodynamics: A Tutorial, in Magnetospheric Current Systems. American Geophysical Union, Washington, D.C. (Geophysical Monograph 118) p. 131.

Roelof, E.C., Sibeck, D.G., 1993. Magnetopause shape as a bivariate function of interplanetary magnetic field *Bz* and solar wind dynamic pressure. J. Geophys. Res. 98, 21,241.

Siscoe, G.L., 1983. Solar system magnetohydrodynamics. In: Carovillano, R.L., Forbes, J.M. (Eds.), Solar-Terrestrial Physics. D. Reidel Pub. Co., Dordrecht, pp. 11–100.

Siscoe, G.L., Erickson, G.M., Sonnerup, B.U.Ö., Maynard, N.C., Schoendorf, J.A., Siebert, K.D., White, W.W., Wilson, G.R., 2002. Hill model of transpolar potential saturation: comparison with MHD simulations. J. Geophys. Res. 107 (A6), 1075.

Smith, C.W., Acuna, M.H., Burlaga, L.F., L'Heureux, J., Ness, N.F., Scheifele, J., 1998. The ACE magnetic field experiment. Space Sci. Rev. 86, 613.

Stern, D.P., 2005. A Historical introduction to the ring current. In: The Inner Magneto-Sphere: Physics and Modeling. American Geophysical Union, Washington, D.C., p. 1 (Geophysical Monograph Series 155).

Storz, M.F., Bowman, B.R., Branson, J.I., 2002. High accuracy satellite drag model (HASDM), AAS/AIAA Astrodynamics Specialist Conference, AIAA 2002–4886, Monterey, CA, 2002.

Tapley, B.D., Bettadpur, S., Watkins, M., Reigber, C., 2004. The gravity recovery and climate experiment: mission overview and early results. Geophys. Res. Lett. 31, L09607.

Weimer, D.R., 1995. Models of high latitude electric potentials derived with a least error fit of spherical harmonic coefficients. J. Geophys. Res. 100, 19,595.

Weimer, D.R., 2001. Maps of ionospheric field-aligned currents as a function of the interplanetary magnetic field from dynamics explorer 2 data. J. Geophys. Res. 1060, 12,889.

Weimer, D.R., 2005. Improved ionospheric electrodynamic models and application to calculating Joule heating rates. J. Geophys. Res. 110, A05306.

Wilson, G.R., Weimer, D.R., Wise, J.O., Marcos, F., 2006. Response of the thermosphere to Joule heating and particle precipitation. J. Geophys. Res. 111, A10314.